AIAA JOURNAL
Vol. 45, No. 6, June 2007

Fast Prediction of Transonic Aeroelastic Stability and Limit Cycles

M. A. Woodgate* and K. J. Badcock†
University of Liverpool, Liverpool, L3 9TY England, United Kingdom.

DOI: 10.2514/1.25604

The exploitation of computational fluid dynamics for aeroelastic simulations is mainly based on time-domain simulations. There is an intense research effort to overcome the computational cost of this approach. Significant aeroelastic effects driven by nonlinear aerodynamics include the transonic flutter dip and limit-cycle oscillations. The paper describes the use of Hopf bifurcation and center manifold theory to compute flutter speeds and limit-cycle responses of wings in transonic flow when the aerodynamics are modeled by the Euler equations. The cost of the calculations is comparable to steady-state calculations based on computational fluid dynamics. The paper describes two methods for finding stability boundaries and then an approach to reducing the full-order system to two degrees of freedom in the critical mode. Details of the three methods are given, including the calculation of first, second, and third Jacobians and the solution of sparse linear systems. Results for the AGARD wing, a supercritical transport type of wing, and the limit-cycle response of the Goland wing are given.

Nomenclature

A	=	Jacobian matrix of $\mathbf{R}$ with respect to $\mathbf{w}$
B, C	=	second and third Jacobian operators
h	=	(scalar) increment for finite differences
F	=	quadratic and higher terms in $\mathbf{R}$
G	=	Taylor coefficients of the residual restricted to the critical eigenspace
H	=	Taylor coefficients of the residual restricted to the noncritical eigenspace
f	=	convective flux discretization
k_{ij}	=	coefficients in center manifold expansion of y
P	=	right eigenvector of A, $\mathbf{P}_1 + i\mathbf{P}_2$
$\mathbf{Q}$	=	left eigenvector of A, $\mathbf{Q}_1 + i\mathbf{Q}_2$
$\mathbf{q}_s$	=	constant scaling vector for the augmented system
$\mathbf{R}$	=	residual vector
v	=	vector for the matrix-free product
$\mathbf{w}$	=	vector of unknowns
y	=	part of $\mathbf{w}$ in the noncritical eigenspace
z	=	part of $\mathbf{w}$ in the critical eigenspace
Δt	=	time step
λ_i	=	sequence of eigenvalues in the inverse power method
μ	=	bifurcation parameter (dynamic pressure)
ω	=	frequency of critical eigenvalue or shift for the inverse power method

Subscripts

A	=	augmented system
f	=	fluid model
s	=	structural model
$\mathbf{w}$, μ	=	indicating differentiation with respect to $\mathbf{w}$ or μ
0	=	equilibrium solution
i, j	=	flux interface i, j
l	=	left interpolated value at an interface
r	=	right interpolated value at an interface

Superscripts

n	=	time level
$\bar{\mathbf{P}}$, $\bar{\mathbf{Q}}$, $\bar{z}$	=	complex conjugate
$\bar{\mathbf{w}}$, $\bar{\mu}$	=	difference from equilibrium solution

Received 5 June 2006; revision received 20 December 2006; accepted for publication 2 January 2007.

*Research Assistant, Computational Fluid Dynamics Laboratory, Flight Sciences Technology, Department of Engineering.

†Professor, Computational Fluid Dynamics Laboratory, Flight Sciences Technology, Department of Engineering; K.J.Badcock@liverpool.ac.uk. Member AIAA.

I. Introduction

LIMIT-CYCLE oscillations (LCOs) have become one central focus in aircraft aeroelasticity. A major reason for this is the widely reported LCO experienced (and tolerated) on the F-16 in certain store configurations [1]. The source of the LCO is still a matter of conjecture, with nonlinear aerodynamics and structural dynamics being considered [2]. Predating the first report of an LCO on the F-16 was the residual pitch oscillation for the B2 bomber , which was attributed to an interaction between the wing-bending mode, a shock movement on the upper surface, and the control system. It seems likely that LCOs have arisen (but have not been reported in the open literature) on other high-performance aircraft.

LCOs can be tolerated (as illustrated by the F-16 example) if the amplitude is sufficiently low. Detrimental effects may accrue to the pilot and the airframe, but the onset of LCO does not necessarily threaten the integrity of the airframe as linear flutter would. It has been suggested that future aircraft may even tolerate regions of LCO in return for gains in performance.

To tolerate or eliminate LCOs requires reliable analysis tools to provide physical insight into mechanisms and requires quantitative predictions. If nonlinear aerodynamics is involved, then a general-purpose tool should exploit computational fluid dynamics (CFD). CFD simulations of aeroelastic behavior in the time domain have reached an impressive level of maturity. Farhat et al. [4] did fundamental work on the numerical methods underpinning such a simulation. Melville [5] used high-fidelity CFD to reproduce LCO behavior for the F-16. A similarly impressive effort was undertaken at the National Aerospace Laboratory/NLR [6]. With this type of capability available, it is perhaps disappointing that more insight was not gained into the F-16 LCO phenomenon through simulation.

Although time-domain simulations are a powerful and general tool for analysis, they suffer from one practical disadvantage: namely, computational cost. For an analysis of an engineering problem, it is likely that a parametric search and sensitivity analysis will be required. If this must be done carrying the cost of time-domain simulations, then the overall cost is likely to be prohibitive.

This has stimulated an active research area in reduced-order modeling. The aim is to retain the predictive capability of full CFD aerodynamics, but with reduced computational cost. Two broad classes of method have appeared: namely, data-driven models and methods that work with the system residual. For data-driven models, a number of forced-motion CFD calculations are computed. The aerodynamic response is then processed to provide a low-order model. Examples include proper orthogonal decomposition [7,8] and a Volterra series [9]. The disadvantages of these approaches is the lack of a general robust parameterization of the model and their inability to predict any physics that is not included in the training data. This class of method has met with some success.

Methods that work with the residual are preferred in the current paper. The general philosophy is to augment the coupled system residual with additional information about the system behavior that allows a reduction in the computational cost. The advantage of doing this is that the predictive capability of the full-order system is retained. The disadvantage is the added technical complication of manipulating the system. The harmonic balance method [2] is being exploited for F-16 LCO.

The research effort that is advanced in the current paper is based on the initial work of [10] to exploit Hopf-bifurcation theory to allow behavior to be determined from the eigenspectrum of the system Jacobian matrix. Various techniques were developed to make this approach robust for airfoil problems [11] and then to allow the extension of the approach to three-dimensional problems [12]. A reduced-order model for damping was developed in this framework [13].

The current paper represents the final step in the basic method development within this research effort. Application to large-scale problems would be the next logical step. Terms are added to the damping model to allow the prediction of LCOs. To facilitate the derivation of the model coefficients, advances in the calculation of the first, second, and third Jacobian matrices and in the linear solver were required and are described.

The paper continues with an overview of the approach to computing reduced models for LCO prediction. The methods are considered, followed by a description of the Jacobian and linear solver algorithms used. Results are then presented for the AGARD, MDO, and Goland wings, with conclusions drawn on computational cost. Finally, overall conclusions and future work are described.

Formulation of Methods

Overview

The strategy to be adopted is first described. All of the methods rely on the CFD and structural residuals, and so the formulation of the time-domain solver is first described. Then, either the inverse power method or the direct bifurcation solver are used to explore the system stability and to find the bifurcation point. As part of this calculation, the critical eigenvalue and eigenvector are computed. Finally, the full system is projected onto the critical eigenvector to obtain a two-degree-of-freedom system that can predict the postcritical response. The aim is to implement all of these steps so that a complete analysis can be performed at an equivalent cost of a small number of steady-state coupled-system solutions. More details on each step are now given.

Coupled Fluid-Structure Time-Domain Solver

The starting point for this work is a time-domain code that was applied to a variety of problems, up to and including the aeroelastic behavior of a jet fighter [14,15]. The current work develops the methods for the Euler equations, and these are formulated in conservative form on time-varying curvilinear coordinates. The main features of the CFD solver are described in [16]. A fully implicit steady solution of the Euler equations is obtained by advancing the solution forward in time by solving the discrete nonlinear system of equations:

$$\frac{\mathbf{w}_f^{n+1} - \mathbf{w}_f^n}{\Delta t} = \mathbf{R}_f\left(\mathbf{w}_f^{n+1}\right) \tag{1}$$

The term on the right-hand side, called the residual,[‡] is the discretization of the convective terms, given here by Osher's approximate Riemann solver [17], MUSCL interpolation [18], and Van Albada's limiter. Equation (1) is a nonlinear system of algebraic equations that is solved by an implicit method [16], the main features of which are an approximate linearization to reduce the size and condition number of the linear system and the use of a preconditioned Krylov subspace method to calculate the updates. The steady-state solver is applied to unsteady problems within a pseudo-time-stepping iteration [19].

The wing deflections are defined at a set of points by a sum of modes derived from a finite element model (FEM) multiplied by their coordinates. The equations for the modal coordinates involve forces that are derived from the CFD solution. For a dynamic calculation, the structural and fluid equations are sequenced in pseudotime, resulting in a properly sequenced solution in real time. The aerodynamic forces are calculated at face centers on the aerodynamic-surface grid. The problem of communicating these forces to the structural grid is complicated in the common situation that these grids are not defined on the same surface. This problem, and the influence it can have on the aeroelastic response, was considered in [20,21], in which a method was developed, called the constant volume tetrahedron (CVT) transformation. This method uses a combination of projection of fluid points onto the structural grid, transformation of the projected point, and recovery of the out-of-plane component to obtain a cheap but effective relation between deformations on the structural and fluid grids.

The geometries of interest deform during the motion. This means that the aerodynamic mesh must be deformed. This is achieved using transfinite interpolation (TFI) of displacements within the blocks containing the wing. More elaborate treatments that move blocks to maintain grid orthogonality are possible [22] but are not necessary here, because only small wing deflections are encountered and the blocks in the mesh can be extended well away from the wing. The wing surface deflections, obtained from the transformation of those calculated on the structural grid, are interpolated to the volume-grid points using a TFI blending function [23]. The grid speeds can be obtained by differentiating the TFI equation to obtain their explicit dependence on the values of the modal velocities.

Direct Solution of Stability Boundary

The semidiscrete form of the coupled CFD-FEM system is

$$\frac{\mathrm{d}\mathbf{w}}{\mathrm{d}t} = \mathbf{R}(\mathbf{w}, \mu) \tag{2}$$

where

$$\mathbf{w} = [\mathbf{w}_f, \mathbf{w}_s]^T \tag{3}$$

is a vector containing the fluid unknowns $\mathbf{w}_f$ and the structural unknowns $\mathbf{w}_s$, and

$$\mathbf{R} = [\mathbf{R}_f, \mathbf{R}_s]^T \tag{4}$$

is a vector containing the fluid residual $\mathbf{R}_f$ and the structural residual $\mathbf{R}_s$. The residual also depends on a parameter μ that is independent of $\mathbf{w}$. An equilibrium of this system $\mathbf{w}_0(\mu)$ satisfies $\mathbf{R}(\mathbf{w}_0, \mu) = \mathbf{0}$.

Dynamic systems theory gives criteria for an equilibrium to be stable [24]. In particular, all eigenvalues of the Jacobian matrix of Eq. (2), given by $A = \partial\mathbf{R}/\partial\mathbf{w}$, must have a negative real part. A Hopf bifurcation with respect to the parameter μ occurs in the stability of the equilibrium at values of μ, such that $A(\mathbf{w}_0, \mu)$ has an eigenvalue $\pm i\omega$ that crosses the imaginary axis. Denoting the corresponding eigenvector by $\mathbf{P} = \mathbf{P}_1 + i\mathbf{P}_2$, a critical value of μ is one at which there is an eigenpair $\pm i\omega$ and $\mathbf{P}$, such that

$$A\mathbf{P} = i\omega\mathbf{P} \tag{5}$$

[‡]The sign of the residual is opposite of convention in CFD, but this is to provide a system of ordinary differential equations that follows the convention of dynamic systems theory.

This equation can be written in terms of real and imaginary parts as $A\mathbf{P}_1 + \omega\mathbf{P}_2 = \mathbf{0}$ and $A\mathbf{P}_2 - \omega\mathbf{P}_1 = \mathbf{0}$. A unique eigenvector is chosen by scaling against a constant real vector $\mathbf{q}_s$ to produce a fixed complex value, taken to be $0 + 1i$. This yields two additional scalar equations: $\mathbf{q}_s^T\mathbf{P}_1 = 0$ and $\mathbf{q}_s^T\mathbf{P}_2 - 1 = 0$.

A bifurcation point can be calculated directly by solving the system of equations

$$\mathbf{R}_A(\mathbf{w}_A) = \mathbf{0} \tag{6}$$

where

$$\mathbf{R}_A = \begin{bmatrix} \mathbf{R} \\ A\mathbf{P}_1 + \omega\mathbf{P}_2 \\ A\mathbf{P}_2 - \omega\mathbf{P}_1 \\ \mathbf{q}_s^T\mathbf{P}_1 \\ \mathbf{q}_s^T\mathbf{P}_2 - 1 \end{bmatrix} \tag{7}$$

and $\mathbf{w}_A = [\mathbf{w}, \mathbf{P}_1, \mathbf{P}_2, \mu, \omega]^T$. If there are n components in $\mathbf{w}$, then $\mathbf{w}_A$ has $3n + 2$ components, as does $\mathbf{R}_A$, and hence Eq. (6) is closed.

Newton's method can be used to solve this type of problem. A sequence of approximations $\mathbf{w}_A^n$ to a solution is generated by solving the linear system

$$\frac{\partial \mathbf{R}_A}{\partial \mathbf{w}_A}\Delta\mathbf{w}_A = -\mathbf{R}_A^n \tag{8}$$

where $\Delta\mathbf{w}_A = \mathbf{w}_A^{n+1} - \mathbf{w}_A^n$. The Jacobian matrix on the left-hand side of Eq. (8) is given in expanded form as

$$\frac{\partial \mathbf{R}_A}{\partial \mathbf{w}_A} = \begin{bmatrix} A & 0 & 0 & \mathbf{R}_\mu & 0 \\ (A\mathbf{P}_1)_\mathbf{w} & A & I\omega & (A\mathbf{P}_1)_\mu & \mathbf{P}_2 \\ (A\mathbf{P}_2)_\mathbf{w} & -I\omega & A & (A\mathbf{P}_2)_\mu & -\mathbf{P}_1 \\ 0 & \mathbf{q}_s^T & 0 & 0 & 0 \\ 0 & 0 & \mathbf{q}_s^T & 0 & 0 \end{bmatrix} \tag{9}$$

A key simplification in Eq. (9) arises when the equilibrium is independent of the bifurcation parameter. In this case, $\mathbf{w}$ can be precalculated and the first row and column can be removed from the matrix in the Newton iteration. This is important because it means that the second Jacobian term does not need to be calculated.

Another consideration for applying this approach is that a good initial condition is required (in particular, a good guess for the eigenvector). To deal with nonsymmetric systems and to allow the calculation of an initial guess, a second method, the inverse power method, is useful. This is described next.

The full details on the implementation of the direct method were developed in [11,12].

Shifted Inverse Power Method

The power method [25] is an algorithm for calculating the dominant eigenvalue–eigenvector pair of any given diagonalizable matrix A. Its extension to the shifted inverse power method is practical for finding any eigenvalue, provided that a good initial approximation to the eigenvalue is known. Assume that the $n \times n$ matrix A has distinct eigenvalues $\lambda_1, \lambda_2, \ldots, \lambda_n$ and consider the eigenvalue λ_j. Then a constant ω can be chosen so that $1/(\lambda_j - \omega)$ is the dominant eigenvalue of $(A - \omega I)^{-1}$. The method can be formulated to involve an iteration on the matrix

$$\begin{bmatrix} A & I\omega \\ -I\omega & A \end{bmatrix} \tag{10}$$

which is identical to the core part of Eq. (9).

The Hopf-bifurcation calculation can proceed as follows. First, linear aeroelastic theory can be used to calculate the bifurcation value and frequency at a subsonic Mach number. This frequency can be used in the inverse power method as a shift to allow the calculation of the eigenvector. These values can then be used as a starting solution for the Newton iterations. Once one Mach number is converged, this solution can be used as an initial guess for the next Mach number. In this way, a stability boundary can be traced out.

A second way of applying the inverse power method is to use it to trace the behavior of an aeroelastic eigenvalue as the bifurcation value is changed. In a manner similar to linear methods, for each structural mode, the structural frequency is used as a shift and the corresponding aeroelastic eigenvalue is calculated. This can then be used as a shift at the next parameter value, and so on. The damping of each mode can be traced.

Model Reduction for LCO Calculation

Finally, the response of the system after bifurcation may be required, particularly if it is a limit-cycle oscillation (LCO). Consider the nonlinear system of Eq. (2). We assume that the Jacobian matrix A has a complex conjugate pair of eigenvalues $\lambda_{1,2} = \pm i\omega$ on the imaginary axis, with the rest having negative imaginary parts. Let $\mathbf{Q}$ and $\mathbf{P}$ be the left and right eigenvectors of A. Then

$$A\mathbf{P} = i\omega\mathbf{P}, \qquad A\bar{\mathbf{P}} = -i\omega\bar{\mathbf{P}}$$

and

$$A^T\mathbf{Q} = -i\omega\mathbf{Q}, \qquad A^T\bar{\mathbf{Q}} = i\omega\bar{\mathbf{Q}}$$

These can be normalized so that $\langle \mathbf{P}, \mathbf{Q} \rangle = 1$, where

$$\langle \mathbf{P}, \mathbf{Q} \rangle = \sum_{i=1}^{n} \bar{P}_i Q_i$$

It is possible to decompose any $\mathbf{w} \in \Re^n$ as

$$\mathbf{w} = z\mathbf{Q} + \bar{z}\bar{\mathbf{Q}} + y$$

where $z \in C^1$, $z\mathbf{Q} + \bar{z}\bar{\mathbf{Q}}$ is in the space corresponding to the critical eigenvalue, and y is in the space spanned by all of the noncritical eigenvalues. Equation (2) then takes the form

$$\begin{cases} z = \langle \mathbf{P}, \mathbf{w} \rangle \\ y = \mathbf{w} - \langle \mathbf{P}, \mathbf{w} \rangle\mathbf{Q} - \langle \bar{\mathbf{P}}, \mathbf{w} \rangle\bar{\mathbf{Q}} \end{cases}$$

because $\langle \mathbf{P}, \bar{\mathbf{Q}} \rangle = 0$ and hence

$$\begin{cases} \dot{z} = i\omega z + \langle \mathbf{P}, F(z\mathbf{Q} + \bar{z}\bar{\mathbf{Q}} + y, \bar{\mu}) \\ \dot{y} = Ay + F(z\mathbf{Q} + \bar{z}\bar{\mathbf{Q}} + y, \bar{\mu}) - \langle \mathbf{P}, F(z\mathbf{Q} + \bar{z}\bar{\mathbf{Q}} + y, \bar{\mu}) \rangle\mathbf{Q} - \langle \mathbf{P}, F(z\mathbf{Q} + \bar{z}\bar{\mathbf{Q}} + y, \bar{\mu}) \rangle\bar{\mathbf{Q}} \end{cases}$$

where $\mathbf{R}(\mathbf{w}, \mu) = \mathbf{R}(\mathbf{w}_0, \mu) + A\bar{\mathbf{w}} + F(\bar{\mathbf{w}}, \mu)$.

This system is $(n + 2)$-dimensional but we have two constraints on y. The system is Taylor-expanded in z, $\bar{z}$, and y to give the following approximation:

$$\begin{cases} \dot{z} = i\omega z + \frac{1}{2}G_{20}z^2 + G_{11}z\bar{z} + \frac{1}{2}G_{02}\bar{z}^2 + \frac{1}{2}G_{21}z^2\bar{z} + \langle G_{10}, y \rangle z + \langle G_{01}, y \rangle\bar{z} + G_{0\mu} + G_{1\mu}z \ldots \\ \dot{y} = Ay + \frac{1}{2}H_{20}z^2 + H_{11}z\bar{z} + \frac{1}{2}H_{02}\bar{z}^2 + \ldots \end{cases} \tag{11}$$

where $G_{20}, G_{11}, G_{02}, G_{21} \in C^1$ and $G_{01}, G_{10}, H_{ij} \in C^n$ involve inner products of the second and third Jacobian operators and for which a compact form is given later. The terms $G_{0\mu} = \langle \mathbf{P}, \mathbf{R}_\mu \bar{\mu} \rangle$ and $G_{1\mu} = A_\mu \bar{\mu}$ arise from an expansion of the residual in μ and provide the reduced model with a parametrization in μ. All of the scalars and vectors are functions of $\mathbf{R}$ or inner products of $\mathbf{P}$, $\mathbf{R}$, and its derivatives, and this makes the manipulation of the system feasible, even for systems of large dimension.

The center manifold theory says that y varies, at most, quadratically with z in the vicinity of the bifurcation, which can then be expressed as

$$y = k(z, \bar{z}) = \tfrac{1}{2}k_{20}z^2 + k_{11}z\bar{z} + \tfrac{1}{2}k_{02}\bar{z}^2 + \mathcal{O}|z|^3$$

with the constraint $\langle \mathbf{P}, k_{ij} \rangle = 0$. The vectors k_{ij} can be found by substituting this form into the y part of Eq. (11) and equating coefficients, which leads to the linear equations

$$\begin{cases} (2i\omega I - A)k_{20} = H_{20} \\ -Ak_{11} = H_{11} \\ (-2i\omega I - A)k_{02} = H_{02} \end{cases} \tag{12}$$

Now write the restricted equation as

$$\dot{\bar{z}} = i\omega z + \tfrac{1}{2}G_{20}z^2 + G_{11}z\bar{z} + \tfrac{1}{2}G_{02}\bar{z}^2 + \tfrac{1}{2}(G_{21} + 2\langle G_{10}, k_{11}\rangle + \langle G_{01}, k_{20}\rangle)z^2\bar{z} + G_{0\mu} + G_{1\mu}z \ldots$$

If we write the quadratic and higher part of $\mathbf{R}$ [which is $F(\mathbf{w}, \mu)$, in terms of functions $B(x, y)$ and $C(x, y, z)$; a definition and how they are evaluated by finite differences follows], then

$$F(x) = \tfrac{1}{2}B(x, x) + \tfrac{1}{6}C(x, x, x) + \mathcal{O}\|x\|^4$$

and it follows that

$$\langle G_{10}, y\rangle = \langle \mathbf{P}, B(\mathbf{Q}, y)\rangle, \qquad \langle G_{01}, y\rangle = \langle \mathbf{P}, B(\bar{\mathbf{Q}}, y)\rangle$$

and hence the restricted equation is in the form

$$\dot{\bar{z}} = i\omega z + \tfrac{1}{2}G_{20}z^2 + G_{11}z\bar{z} + \tfrac{1}{2}G_{02}\bar{z}^2 + \tfrac{1}{2}(G_{21} - 2\langle \mathbf{P}, B(\mathbf{Q}, A^{-1}H_{11})\rangle + \langle \mathbf{P}, B(\bar{\mathbf{Q}}, (2i\omega I - A)^{-1}H_{20})\rangle)z^2\bar{z} + G_{0\mu} + G_{1\mu}z$$

where

$$\begin{aligned} G_{20} &= \langle \mathbf{P}, B(\mathbf{Q}, \mathbf{Q})\rangle & G_{11} &= \langle \mathbf{P}, B(\mathbf{Q}, \bar{\mathbf{Q}})\rangle \\ G_{02} &= \langle \mathbf{P}, B(\bar{\mathbf{Q}}, \bar{\mathbf{Q}})\rangle & G_{21} &= \langle \mathbf{P}, C(q, q, \bar{\mathbf{Q}})\rangle \end{aligned} \tag{13}$$

and

$$\begin{cases} H_{20} = B(\mathbf{Q}, \mathbf{Q}) - \langle \mathbf{P}, B(\mathbf{Q}, \mathbf{Q})\rangle\mathbf{Q} - \langle \bar{\mathbf{P}}, B(\mathbf{Q}, \mathbf{Q})\rangle\bar{\mathbf{Q}} \\ H_{11} = B(\mathbf{Q}, \bar{\mathbf{Q}}) - \langle \mathbf{P}, B(\mathbf{Q}, \bar{\mathbf{Q}})\rangle\mathbf{Q} - \langle \bar{\mathbf{P}}, B(\mathbf{Q}, \bar{\mathbf{Q}})\rangle\bar{\mathbf{Q}} \end{cases}$$

This is a two-degree-of-freedom system for the response of the full-order system in the critical mode, and because it contains terms that are cubic in z, it should be able to predict limit-cycle behavior after the bifurcation. The reduced model is calculated once and for all after the critical eigenvector, eigenvalue, and equilibrium are known. The model is parametrized through the Taylor expansion in the bifurcation parameter, and so it can be used to explore the behavior of the full system in the vicinity of the bifurcation. The main work in forming the model is in the matrix-vector products against the second and third Jacobians, and this will be discussed later. The linear systems that need to be solved to compute the coefficients in the center manifold reduction are solved in the same manner as for the inverse power method, as discussed next.

Linear Solver

A crucial task in the three algorithms described earlier is the solution of a large sparse linear system. Eisenstat et al. [26] developed a generalized conjugate gradient method, called the generalized conjugate residual (GCR) algorithm. The crucial factor for the efficiency of such a method is the preconditioning used. This is described in the current section. Note that the Jacobian matrix consists of 5×5 blocks and that these are considered as the basic matrix element in the current section.

Consider a general sparse matrix A for which the elements are a_{ij} $(i,\ j = 1, \ldots, n)$. A general incomplete factorization computes a sparse lower triangular matrix L and a sparse upper triangular matrix U so that the residual matrix $LU - A$ satisfies certain constraints, such as having entries in a prescribed pattern. A common constraint consists of taking the zero pattern of the LU factors to be precisely the zero pattern of A. However, the accuracy of the $ILU(0)$ incomplete factorization may be insufficient to provide an adequate rate of convergence.

More accurate block incomplete LU (BILU) factorizations that allow extra terms to be filled into the factorization are often more efficient as well as more robust. Consider updating the a_{ij} element in full Gaussian elimination (GE). The inner loop contains the equation

$$a_{ij} = a_{ij} - a_{ik}a_{kj} \tag{14}$$

If lev_{ij} is the current level of element a_{ij}, then the new level is defined to be

$$\text{lev}_{\,ij} = \min(\text{lev}_{ij}, \text{lev}_{ik} + \text{lev}_{kj} + 1) \tag{15}$$

The initial level of fill-in for an element a_{ij} of a sparse matrix A is 0 if $a_{ij} \neq 0$ and is ∞ otherwise. Each time the element is modified in the GE process, its level of fill-in is updated by Eq. (15). Observe that the level of fill-in of an element will never increase during the elimination. Thus, if $a_{ij} \neq 0$ in the original matrix A, then the element will have a level of fill-in equal to zero throughout the elimination process. The preceding gives a systematic algorithm for discarding elements. Hence, $ILU(k)$ contains all of the fill-in elements for which the level of fill-in does not exceed k.

The current work used both the real and complex variable versions of the GCR and BILU algorithms. The complex version can be used for the inverse power method and has the advantage that the terms in the coefficient matrix arising from the shift are concentrated on the (complex) diagonal and are not scattered to the top right and bottom left blocks, as in the real variable case. This is advantageous in terms of concentrating fill-in where it is required. For the AGARD wing test case computed later, it was observed that the number of nonzero blocks in the BILU factorization when using complex rather than real variables reduced by a factor of 0.44, 0.37, and 0.32 when using 1, 2, and 3 levels of fill-in. The increase in the number of terms in the real preconditioner did not translate into a significant reduction in the number of iterations to convergence. The complex formulation is therefore used with the inverse power and center manifold methods, with the real formulation used for the direct solver. In all cases, the performance of the linear solver was observed to be good, with fully converged solutions obtained in no more than 100–200 iterations, and normally much less.

Calculation of First, Second, and Third Jacobians

Analytical Terms for the First Jacobian

The calculation of the first Jacobian A is most conveniently done by partitioning the matrix as

$$A = \begin{bmatrix} \frac{\partial \mathbf{R}_f}{\partial \mathbf{w}_f} & \frac{\partial \mathbf{R}_f}{\partial \mathbf{w}_s} \\ \frac{\partial \mathbf{R}_s}{\partial \mathbf{w}_f} & \frac{\partial \mathbf{R}_s}{\partial \mathbf{w}_s} \end{bmatrix} = \begin{bmatrix} A_{ff} & A_{fs} \\ A_{sf} & A_{ss} \end{bmatrix} \tag{16}$$

The block A_{ff} describes the influence of the fluid unknowns on the fluid residual and has by far the largest number of nonzeros when a modal structural model is used. The treatment of this term is crucial to

the efficiency of the scheme and is discussed later. The meaning and calculation of the other terms is described in detail in [12].

In previous work, the analytical calculation of A_{ff} had only been made for a first-order spatial discretization. This prevented quadratic convergence from being obtained from the direct solver, did not allow the inverse power method to be used for the case when a second-order spatial scheme was used and would not allow the use of the center manifold expression for y. It is therefore important that this limitation is removed, and this is described later.

The residual for one cell in the grid is built up from fluxes. Following the usual approach for Riemann solvers,

$$\mathbf{f}_{i,j} = \mathbf{f}_{i,j}(\mathbf{w}_l, \mathbf{w}_r)$$

where $\mathbf{w}_l = \mathbf{w}_l(\mathbf{w}_{i-2,j}, \mathbf{w}_{i-1,j}, \mathbf{w}_{i,j}, \mathbf{w}_{i+1,j})$ and $\mathbf{w}_r = \mathbf{w}_r(\mathbf{w}_{i-1,j}, \mathbf{w}_{i,j}, \mathbf{w}_{i+1,j}, \mathbf{w}_{i+2,j})$. Here, $\mathbf{f}_{i,j}$ is computed using Osher's [17] approximate Riemann solver. The left and right states are computed from the cell values using MUSCL interpolation. For the cell interface we are considering, there are four contributions to the Jacobian matrix, arising from

$$\frac{\partial \mathbf{f}_{i,j}}{\partial \mathbf{w}_{i-2,j}}, \qquad \frac{\partial \mathbf{f}_{i,j}}{\partial \mathbf{w}_{i-1,j}}, \qquad \frac{\partial \mathbf{f}_{i,j}}{\partial \mathbf{w}_{i,j}}, \qquad \frac{\partial \mathbf{f}_{i,j}}{\partial \mathbf{w}_{i+1,j}}$$

Now, for the approximate Jacobian that can be used to drive convergence of the Newton iterations, the following approximations were made:

$$\frac{\partial \mathbf{f}_{i,j}}{\partial \mathbf{w}_{i-2,j}} \approx \mathbf{0}; \qquad \frac{\partial \mathbf{f}_{i,j}}{\partial \mathbf{w}_{i-1,j}} \approx \frac{\partial \mathbf{f}_{i,j}}{\partial \mathbf{w}_l}; \qquad \frac{\partial \mathbf{f}_{i,j}}{\partial \mathbf{w}_{i,j}} \approx \frac{\partial \mathbf{f}_{i,j}}{\partial \mathbf{w}_r}$$

$$\frac{\partial \mathbf{f}_{i,j}}{\partial \mathbf{w}_{i+1,j}} \approx \mathbf{0}$$

These approximations are exact for a first-order spatial discretization where $\mathbf{w}_l = \mathbf{w}_{i-1,j}$ and $\mathbf{w}_r = \mathbf{w}_{i,j}$. The calculation of the terms

$$\frac{\partial \mathbf{f}_{i,j}}{\partial \mathbf{w}_l}$$

and

$$\frac{\partial \mathbf{f}_{i,j}}{\partial \mathbf{w}_r}$$

is nontrivial but was coded, tested, and used in the CFD solver [16]. These are exploited to calculate the exact Jacobian terms for the second-order spatial discretization by using the chain rule

$$\frac{\partial \mathbf{f}_{i,j}}{\partial \mathbf{w}_{i-2,j}} = \frac{\partial \mathbf{f}_{i,j}}{\partial \mathbf{w}_l}\frac{\partial \mathbf{w}_l}{\partial \mathbf{w}_{i-2,j}} \qquad \frac{\partial \mathbf{f}_{i,j}}{\partial \mathbf{w}_{i-1,j}} = \frac{\partial \mathbf{f}_{i,j}}{\partial \mathbf{w}_l}\frac{\partial \mathbf{w}_l}{\partial \mathbf{w}_{i-1,j}} + \frac{\partial \mathbf{f}_{i,j}}{\partial \mathbf{w}_r}\frac{\partial \mathbf{w}_r}{\partial \mathbf{w}_{i-1,j}}$$

$$\frac{\partial \mathbf{f}_{i,j}}{\partial \mathbf{w}_{i,j}} = \frac{\partial \mathbf{f}_{i,j}}{\partial \mathbf{w}_l}\frac{\partial \mathbf{w}_l}{\partial \mathbf{w}_{i,j}} + \frac{\partial \mathbf{f}_{i,j}}{\partial \mathbf{w}_r}\frac{\partial \mathbf{w}_r}{\partial \mathbf{w}_{i,j}} \qquad \frac{\partial \mathbf{f}_{i,j}}{\partial \mathbf{w}_{i+1,j}} = \frac{\partial \mathbf{f}_{i,j}}{\partial \mathbf{w}_r}\frac{\partial \mathbf{w}_r}{\partial \mathbf{w}_{i+1,j}}$$

Some care must be taken at boundaries for which halo cells are used to simplify implementation. The halo values are functions of the internal values $\mathbf{w}_{b1} = \mathbf{w}_{b1}(\mathbf{w}_1, \mathbf{w}_2)$ and $\mathbf{w}_{b2} = \mathbf{w}_{b2}(\mathbf{w}_1, \mathbf{w}_2)$ with the exact relationship depending on the type of boundary. Applying the chain rule,

$$\frac{\partial \mathbf{f}_b}{\partial \mathbf{w}_1} = \frac{\partial \mathbf{f}_b}{\partial \mathbf{w}_l}\frac{\partial \mathbf{w}_l}{\partial \mathbf{w}_1} + \frac{\partial \mathbf{f}_b}{\partial \mathbf{w}_r}\frac{\partial \mathbf{w}_r}{\partial \mathbf{w}_1} + \frac{\partial \mathbf{f}_b}{\partial \mathbf{w}_l}\frac{\partial \mathbf{w}_l}{\partial \mathbf{w}_{b1}}\frac{\partial \mathbf{w}_{b1}}{\partial \mathbf{w}_1} + \frac{\partial \mathbf{f}_b}{\partial \mathbf{w}_r}\frac{\partial \mathbf{w}_r}{\partial \mathbf{w}_{b1}}\frac{\partial \mathbf{w}_{b1}}{\partial \mathbf{w}_1} + \frac{\partial \mathbf{f}_b}{\partial \mathbf{w}_l}\frac{\partial \mathbf{w}_l}{\partial \mathbf{w}_{b2}}\frac{\partial \mathbf{w}_{b2}}{\partial \mathbf{w}_1}$$

and

$$\frac{\partial \mathbf{f}_b}{\partial \mathbf{w}_2} = \frac{\partial \mathbf{f}_b}{\partial \mathbf{w}_l}\frac{\partial \mathbf{w}_l}{\partial \mathbf{w}_2} + \frac{\partial \mathbf{f}_b}{\partial \mathbf{w}_r}\frac{\partial \mathbf{w}_r}{\partial \mathbf{w}_2} + \frac{\partial \mathbf{f}_b}{\partial \mathbf{w}_l}\frac{\partial \mathbf{w}_l}{\partial \mathbf{w}_{b1}}\frac{\partial \mathbf{w}_{b1}}{\partial \mathbf{w}_2} + \frac{\partial \mathbf{f}_b}{\partial \mathbf{w}_l}\frac{\partial \mathbf{w}_l}{\partial \mathbf{w}_{b2}}\frac{\partial \mathbf{w}_{b2}}{\partial \mathbf{w}_2}$$

The dependence of the halo values on the interior values also leads to similar extra terms from the adjacent interfaces to the boundary.

The Jacobians of the second-order spatial scheme were tested by forming matrix-vector products against random vectors and comparing with the results from a matrix-free product.

Second and Third Jacobians

The high-order Jacobians required in the model reduction are represented by the bilinear and trilinear functionals

$$B(x, y) = \sum_{j,k=1}^{n} \frac{\partial^2 \mathbf{R}_{(}\xi, \omega)}{\partial \xi_j \xi_k}\bigg|_{\xi = x_0} x_j y_k, \qquad i = 1, 2, \ldots, n \tag{17}$$

and

$$C(x, y, z) = \sum_{j,k,l=1}^{n} \frac{\partial^3 \mathbf{R}_{(}\xi, \omega)}{\partial \xi_j \xi_k \xi_l}\bigg|_{\xi = x_0} x_j y_k z_l, \qquad i = 1, 2, \ldots, n \tag{18}$$

It is possible to calculate all of the contributions to Eqs. (17) and (18) without having to resort to complex arithmetic, or to calculating all the second and third partial derivatives analytically.

Denoting

$$\mathbf{Q} = \mathbf{Q}_1 + i\mathbf{Q}_2, \qquad \mathbf{Q} \in C^n \qquad \mathbf{Q}_1, \mathbf{Q}_2 \in R^n$$

then the following identities can be derived

$$\begin{aligned} B(\mathbf{Q}, \mathbf{Q}) &= B(\mathbf{Q}_1, \mathbf{Q}_1) - B(\mathbf{Q}_2, \mathbf{Q}_2) + 2iB(\mathbf{Q}_1, \mathbf{Q}_2) \\ B(\mathbf{Q}, \bar{\mathbf{Q}}) &= B(\mathbf{Q}_1, \mathbf{Q}_1) + B(\mathbf{Q}_2, \mathbf{Q}_2) \\ C(\mathbf{Q}, \mathbf{Q}, \bar{\mathbf{Q}}) &= C(\mathbf{Q}_1, \mathbf{Q}_1, \mathbf{Q}_1) + C(\mathbf{Q}_1, \mathbf{Q}_2, \mathbf{Q}_2) \\ &\quad + iC(\mathbf{Q}_1, \mathbf{Q}_1, \mathbf{Q}_2) + iC(\mathbf{Q}_2, \mathbf{Q}_2, \mathbf{Q}_2) \end{aligned} \tag{19}$$

Further, the following identities can be derived:

$$\begin{aligned} B(v + w, v + w) &= B(v, v) + 2B(v, w) + B(w, w) \\ B(v - w, v - w) &= B(v, v) - 2B(v, w) + B(w, w) \end{aligned}$$

so that $B(v, w)$ can be expressed as

$$B(v, w) = \tfrac{1}{4}[B(v + w, v + w) - B(v - w, v - w)]$$

A similar set of identities hold for C

$$\begin{aligned} C(v + w, v + w, v + w) &= C(v, v, v) + 3C(v, v, w) \\ &\quad + 3C(v, w, w) + C(w, w, w) \\ C(v - w, v - w, v - w) &= C(v, v, v) - 3C(v, v, w) + 3C(v, w, w) \\ &\quad + C(w, w, w) \end{aligned}$$

and hence $C(v, v, w)$ can be expressed as

$$\begin{aligned} C(v, v, w) = \tfrac{1}{6}[&C(v + w, v + w, v + w) - C(v - w, v - w, v - w) \\ &- 2C(w, w, w)] \end{aligned}$$

By the use of directional derivatives, it is then possible to evaluate the bilinear and trilinear functions $B(x, y)$ and $C(x, y, z)$ on any set of coinciding real vectors. These derivatives can be approximated using finite differences

$$B(v, v) = \frac{1}{h^2}[\mathbf{R}(\mathbf{w}_0 + hv, \mu_0) - \mathbf{R}(\mathbf{w}_0 - hv, \mu_0)] + \mathcal{O}(h^3) \tag{20}$$

and

$$\begin{aligned} C(v, v, v) = \frac{1}{8h^3}&[-\mathbf{R}_3 + 8\mathbf{R}_2 - 13\mathbf{R}_1 + 13\mathbf{R}_{-1} - 8\mathbf{R}_{-2} + \mathbf{R}_{-3}] \\ &+ \mathcal{O}(h^4) \end{aligned} \tag{21}$$

where h is small and $\mathbf{R}_l = \mathbf{R}(\mathbf{w}_0 + lhv, \mu_0)$.

Table 1 Convergence of reduced-order model coefficient real parts under h refinement[a]

Precision	h	G_{20}	G_{02}	G_{21}	k_{11}	k_{20}
d-d	10^{-2}	1.15941e − 03	3.81780e − 04	−6.31471e − 01	−8.57054e − 04	−8.74648e − 04
d-d	10^{-4}	3.83222e − 04	3.04452e − 03	5.28431e + 00	−1.69352e − 03	−1.24885e − 04
d-d	10^{-6}	1.19108e − 03	4.41072e − 04	−1.50604e − 03	−8.36232e − 04	−8.67600e − 04
d-d	10^{-8}	1.19108e − 03	4.41072e − 04	−1.91813e − 03	−8.36232e − 04	−8.67600e − 04
d-d	10^{-10}	1.19108e − 03	4.41070e − 04	3.67596e + 02	−8.36229e − 04	−8.67599e − 04
d-d	10^{-12}	1.12010e − 03	4.57337e − 04	−2.37683e + 08	−8.66090e − 04	−8.97841e − 04
q-d	10^{-2}	1.07216e − 03	4.67501e − 04	−5.96457e − 01	−8.09330e − 04	−8.49737e − 04
q-d	10^{-4}	3.83222e − 04	3.04452e − 03	5.28431e + 00	−1.69352e − 03	−1.24885e − 04
q-d	10^{-6}	1.19108e − 03	4.41072e − 04	−1.50604e − 03	−8.36232e − 04	−8.67600e − 04
q-d	10^{-8}	1.19108e − 03	4.41072e − 04	−1.50604e − 03	−8.36232e − 04	−8.67600e − 04
q-d	10^{-10}	1.19108e − 03	4.41072e − 04	−1.50604e − 03	−8.36232e − 04	−8.67600e − 04
q-d	10^{-12}	1.19108e − 03	4.41072e − 04	−1.50604e − 03	−8.36232e − 04	−8.67600e − 04
q-d	10^{-14}	1.19108e − 03	4.41072e − 04	−1.50604e − 03	−8.36232e − 04	−8.67600e − 04
q-d	10^{-16}	1.19108e − 03	4.41072e − 04	−1.50604e − 03	−8.36232e − 04	−8.67600e − 04
q-d	10^{-18}	1.19108e − 03	4.41072e − 04	−1.52353e − 03	−8.36232e − 04	−8.67600e − 04

[a]The behavior of the real and imaginary parts not shown is identical. Note that all columns include second Jacobian-vector products, except the column for G_{21}, which contains a third Jacobian-vector product. The abbreviations d-d and q-d stand for double-double and quad-double, respectively.

For a first-order Jacobian-vector product,

$$Jv \approx \frac{\mathbf{R}(\mathbf{w} + h_1 v, \mu_0) - \mathbf{R}(\mathbf{w}), \mu_0}{h_1}$$

for some step size h_1. In finite precision, due to rounding errors, we compute $\mathbf{R}(\mathbf{w}, \mu_0) + \epsilon(\mathbf{w})$ instead of $\mathbf{R}(\mathbf{w}, \mu_0)$. Assuming that the rounding error is less that $\bar{\epsilon}$ for all $\mathbf{w}$,

$$Jv - \frac{\mathbf{R}(\mathbf{w} + h_1 v, \mu_0) + \epsilon(\mathbf{w} + h_1 v) - \mathbf{R}(\mathbf{w}, \mu_0) - \epsilon(\mathbf{w})}{h_1} = \mathcal{O}(h_1 + \bar{\epsilon}/h_1)$$

The error is minimized when

$$h_1 = \sqrt{\bar{\epsilon}} \frac{\|\mathbf{w}\|_2}{\|v\|_2}$$

For the third Jacobian, even in the best case in which the components $\mathbf{w}_i$ and v_i are of similar magnitude, the corresponding expression for the optimal step size is $h_3 \approx \sqrt[5]{\bar{\epsilon}}$. For a standard double-precision number, there are 53 bits in the mantissa that leads to $\epsilon = 1/2^{53} \approx 1.11 \times 10^{16}$. Hence, $h_3 = 0.0006$ and, at best, six significant figures can be obtained. However, in general, the answer is less accurate.

One way to increase the accuracy is to increase the number of bits in the mantissa. This can be achieved by using double-double or quad-double arithmetic for the residual evaluation. A high-precision version of algebraic and transcendental functions is also required, in this case, because of the contributions of such functions in Osher's flux function. The QD[§] library was used to obtain this functionality. This library allows extension of existing code to double-double precision and quad-double precision without major recoding, by using operator overloading.

The convergence of the reduced model coefficients under h refinement for the Goland wing example at Mach 0.92 is demonstrated in Table 1. We would expect these coefficients to behave as follows. First, for large values of h, there would be significant inaccuracy due to truncation error. At small values of h, we would see inaccuracy due to rounding error. The latter effect would be more significant for the coefficient that includes a third Jacobian product and less significant using quad-double arithmetic. For a usable method, we need to obtain consistent results over a significant range of h. The table conforms to all of these expectations, and a reliable set of coefficients for the reduced model is obtained.

[§]Available online at crd.lbl.gov/~dhbailey/mpdist/index.html [retrieved 28 February 2006].

Results

Test Cases and Grids

The intention of the current work is to demonstrate the potential of the methods described earlier. For large-scale calculations, a parallel version of the solver is required and this will be discussed in the conclusions. Test cases are therefore required here that are representative of large-scale problems that are targeted, but that can be calculated on a single processor. Three cases were selected and the reasons for each are summarized in the current section.

The AGARD wing is a standard case that is used to benchmark most CFD aeroelastic methods presented in the literature. The case is relatively benign in that it does not feature strong nonlinearity, but many previous computational results are available to add to experimental data. A previous study [12] looked at this case in detail using the direct method, but with the Newton iterations driven by the Jacobian matrix of the first-order spatial scheme. Features of this previous work were the detailed grid-refinement study and related investigations of structural damping, together with an evaluation against published computational results. Grid-converged solutions were presented for the first time in the literature. In the current work, results using the inverse power method and the direct method are obtained using the Jacobian of the second-order spatial scheme. The grid used has 17,900 points (89,000 degrees of freedom) and is comparable to the coarse grid in the previous study. A topology is used that clusters points toward the wing tip that is the most critical area in an aeroelastic calculation of this case. The flutter speed

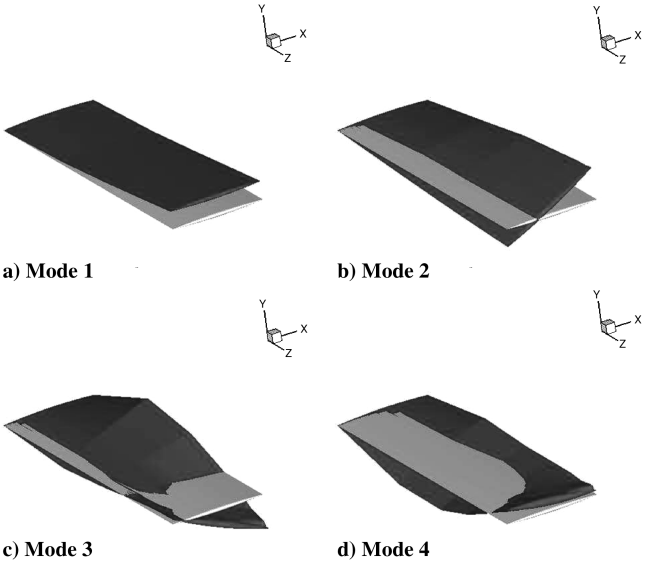

Fig. 1 Structural modes for the Goland wing.

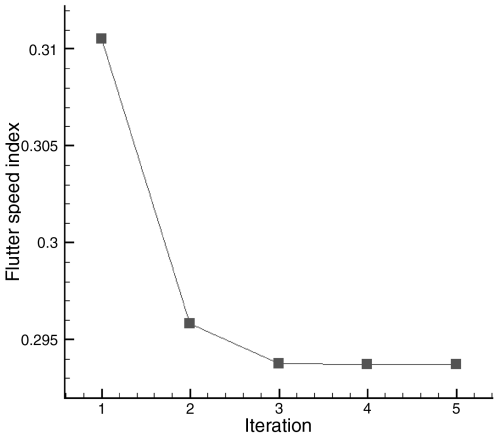

Fig. 2 Convergence of flutter speed index for the AGARD wing at Mach 0.97.

computed on the coarse grid differs by about 4% compared with the grid-converged value.

The MDO wing is a commercial transport wing with a span of 36 m, designed to fly in the transonic regime [27,28]. The profile is a thick supercritical section. The structure is modeled as a wing box running down the central portion of the wing. The structural model consists of eight modes between 0.88 and 14.97 Hz. This case has a nonsymmetric section and so the static solution is dependent on the dynamic pressure, in contrast to the AGARD and Goland cases. The inverse power method is used next to map out the behavior of the eigenspectrum with and without the effect of the static deflection. The grid has 22,000 points (110,000 degrees of freedom) and was derived by extracting points from a finer grid that has 600,000 points. Steady calculations on both grids confirmed that the aerostatic solution and the flow topology obtained, which at Mach 0.85 is an upward bending and nose-down twisting at the wing tip and a strong shock toward the trailing edge that is weakened by the deflection, are similar on both grids, although the coarse-grid solution has a more diffuse suction peak and shock. This case was felt to be a good first test for the inverse power method.

Finally, the most important test case in the current work is the Goland wing. The heavy version of the Goland wing is used to investigate the prediction of LCO behavior. The Goland wing has a chord of 1.8288 m and a span of 6.096 m. It is a rectangular cantilevered wing with a 4% thick parabolic section. The structural model follows the description given in [29]. The case used here has a tip store in the structural model, but not in the aerodynamic model. Four modes were extracted at frequencies (in hertz) of 1.72 (first bending), 3.05 (first torsion), 9.18 (second bending), and 11.10 (second torsion). These modes are shown in Fig. 1.

An interesting feature of this test case is the appearance of a region of limit-cycle oscillation at a reduced value of dynamic pressure (a "bucket") at a freestream Mach number of 0.92. This was shown using the Euler equations [30] and the transonic small disturbance equations [29]. The influence of the tip store was examined in [31] and the effect of including the store aerodynamics in [32].

Following the experience gained with generating grids for the AGARD wing, a grid with 27,000 points (135,000 degrees of

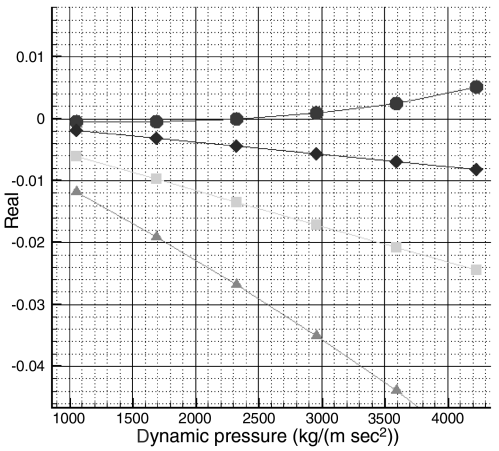

a) Real

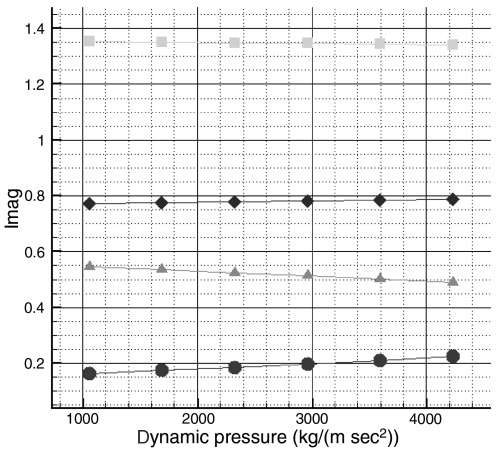

b) Imaginary

Fig. 3 Tracking of eigenvalues for the AGARD wing at Mach 0.97; each line corresponds to one aeroelastic mode and the symbols are consistent between the graphs for the real and imaginary parts.

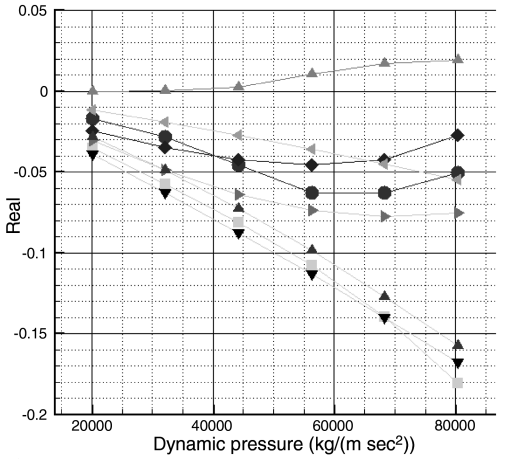

a) Real

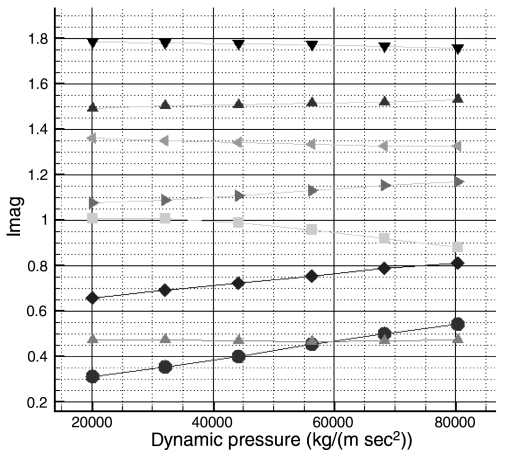

b) Imaginary

Fig. 4 Tracking of eigenvalues for the MDO wing with no initial aerostatic solution at Mach 0.85; each line corresponds to one aeroelastic mode and the symbols are consistent between the graphs for the real and imaginary parts.

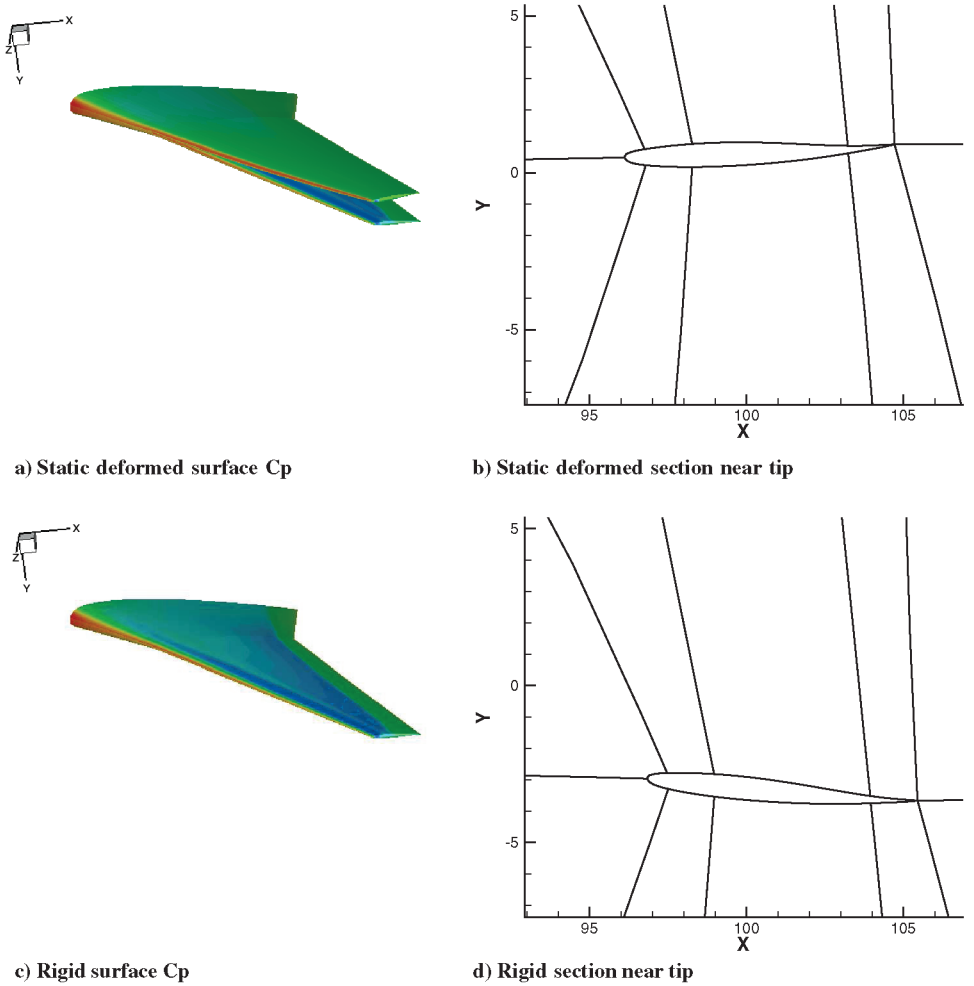

Fig. 5 Surface pressure distribution and tip airfoil section for rigid and static deformed positions of the MDO wing at Mach 0.85.

freedom) was generated using a block topology that concentrates points in the tip region. This grid reproduces the behavior previously reported in the literature: namely, a rising flutter speed around Mach 0.9, a significant bucket with LCO behavior about $M = 0.92$, and then a rise in flutter speed at the right-hand end of the bucket of around 0.94. The values at which these different behaviors happen is similar in the current work, and it is concluded that the current grid for the Goland wing represents a proper test for the methods presented.

AGARD Wing

In [12], the prediction of the flutter boundary by the direct method, using the Jacobian of the first-order scheme to drive the (approximate) Newton method, was compared with time-domain predictions, which were in perfect agreement. A detailed grid-refinement study was undertaken and the first grid-converged solutions were published. The issue of the influence of structural damping on the solution in the dip at Mach 0.97 was considered in detail. Finally, comparison with other published results, including measurements, was made. None of these issues are repeated in the current paper.

The behavior of the direct method when using the full Newton's method and the inverse power method are considered. These investigations are made possible by the availability of the Jacobian matrix of the second-order spatial scheme. The grid used is discussed in the previous section. The four important modes from the structural model, which is of the plate variety, were retained.

The convergence of the flutter speed index at Mach 0.97 is shown in Fig. 2. Rapid convergence is obtained through quadratic convergence of Newton's method, with the critical value being obtained in three iterations. The inverse power method was used to trace out the values of the aeroelastic eigenvalues, which are associated with the structural modes, as a function of dynamic pressure. The real and imaginary parts are shown in Fig. 3. The critical dynamic pressure, which is when the real part of an eigenvalue goes positive, agrees with the value from the direct calculation.

In [13], a simpler version of the reduced model described earlier was developed. In essence, this model completely neglected the influence of the noncritical part of the eigenspace and was designed to calculate damping only. The current approach, which is more general, should reduce to this model below the bifurcation point. The cases from the previous paper were recomputed and this was confirmed.

MDO Wing

This case introduces a new issue compared with the AGARD and Goland cases in that the wing has a significant static deflection. This makes the inverse power method preferable to calculate the flutter point, because this method can naturally take into account the static deformation. The real and imaginary parts of the eigenvalues of the aeroelastic system are plotted in Fig. 4, in which no static deflection is allowed (that is the equilibrium solution is taken about the rigid wing). The dynamic pressure at which the second mode becomes undamped is $28,594\ \text{kg}/(\text{ms}^2)$. The equivalent plot when a static deflection is allowed looks very similar, except that the crossing of the second mode happens at $58,097\ \text{kg}/(\text{ms}^2)$; that is, the effect of the static deflection is to increase the critical dynamic pressure. The reason for this is clear from Fig. 5, in which, as would be expected, the influence of the aerostatic deflection is to bend the wing up and

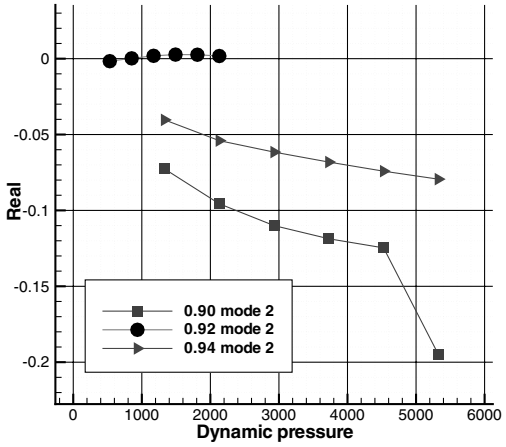

a) Mode 2

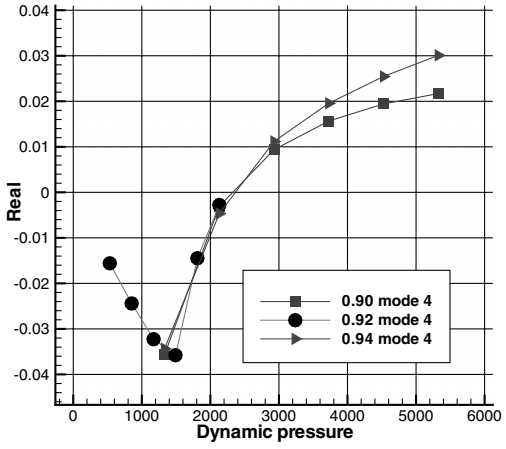

b) Mode 4

Fig. 6 Behavior of the damping of modes 2 and 4 for the Goland wing at Mach 0.92; dynamic pressure is in units of kg/(m s^2).

twist it nose down at the wing tip, as shown in the figure. This weakens the shock, which is likely to be stabilizing for the dynamic behavior. What is important here is that this aerostatic effect is taken into account naturally by the inverse power method, because the Jacobian used is computed at the correct static solution for a given dynamic pressure.

Goland Wing

The steps for a complete analysis of an LCO are now considered. First, the inverse power method is used to investigate the behavior of the structural modes under the influence of transonic aerodynamics. Mach numbers of 0.90, 0.92, and 0.94 were investigated, these values being chosen because of prior knowledge of the system behavior. However, without prior knowledge of the aeroelastic behavior, this Mach number range would have been quickly identified by considering shock wave behavior for the steady-state solutions. Starting with the structural frequency as a shift, the eigenvalue in the aeroelastic system was computed for six values within a range of dynamic pressure, chosen based on linear flutter analysis. The results show that at Mach 0.90 and 0.94, the third and fourth modes interact and the fourth mode eventually crosses the imaginary axis. The behavior of the real part of the fourth mode is shown in Fig. 6, in which it is also seen that the behavior of this mode at Mach 0.92 is very similar. However, at Mach 0.92, the second mode crosses the imaginary axis at a lower dynamic pressure, also shown in Fig. 6, and it is this mode that results in a limit-cycle oscillation.

Having gained some insight into the behavior of the eigenspectrum, the direct method was then used to find the bifurcation point at Mach 0.92. An estimate of the dynamic pressure, frequency, and eigenvector was obtained from the inverse power results. The convergence of the dynamic pressure is shown in Fig. 7 and again shows quadratic convergence.

Finally, the behavior of the limit-cycle oscillation was investigated using the reduced model. The model coefficients were formed using the expressions described earlier, based on the critical eigenvectors, the equilibrium solution and first, second, and third Jacobian-vector products. Time-domain simulations were also run to provide a comparison for the predictions of the reduced model. The time-domain simulations used a reduced time step of 0.5, giving about 70 time steps per period of response, which provides time accuracy at a low computational cost.

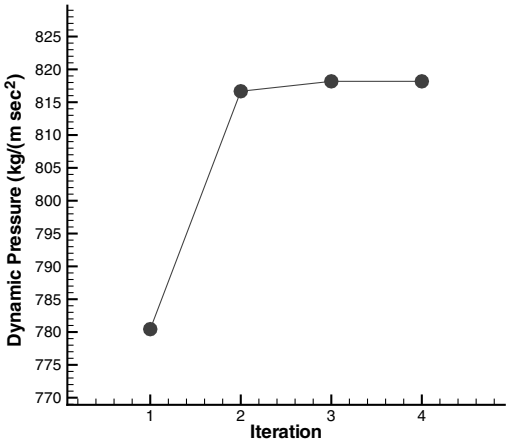

Fig. 7 Convergence of bifurcation parameter for the Goland wing at Mach 0.92.

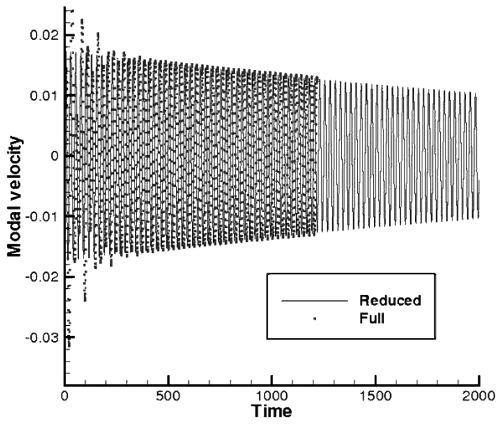

a) 95% of the critical dynamic pressure

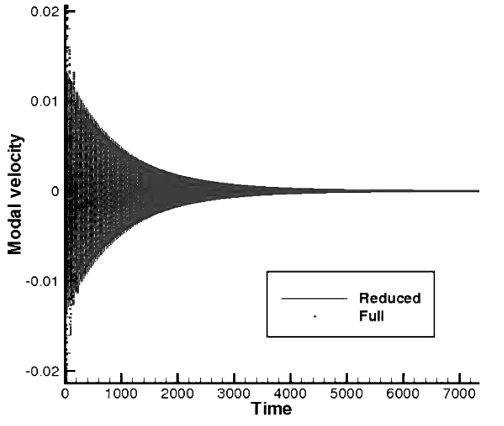

b) 80% of the critical dynamic pressure

Fig. 8 Comparison between the full and reduced predictions of damping for the Goland wing at Mach 0.92.

First, the reduced model predictions are compared with the full model for damped responses. The comparison of the response of the first mode is shown in Fig. 8 at 80 and 95% of the critical dynamic pressure. In both cases, the damped response is well predicted by the reduced model.

The comparison of the reduced and full nonlinear predictions of the LCO response of the first and second structural modes at a value of dynamic pressure that is 25% above the bifurcation value is shown in Fig. 9. The two sets of results agree well. The rise in amplitude with increasing dynamic pressure is shown in Fig. 10, and it is seen that the reduced model predicts well the LCO amplitude for values of dynamic pressure up to 40% above the bifurcation value in this case.

A set of visualizations of the wing location and the difference in pressure from the equilibrium solution is compared in Fig. 11. The wing motion is a combination of plunging and pitching toward the tip, and the fluid response is dominated by changes of pressure toward the leading edge and due to the shock motion. The predictions of the reduced-order model and the full system are very similar qualitatively and quantitatively (note that these two sets of results are plotted on the same scale, with the extreme values being $\pm 4\%$ of the freestream pressure).

Evaluation of Cost

The performance of the methods is assessed in the current section. The benchmark adopted is the cost of a steady-state calculation, because this is generally quite modest on modern computers, and with modern algorithms, even for complex problems. The summary of the cost for the different methods is given in Table 2.

It is noted that the steady solver used here has proved efficient on a wide variety of CFD and aeroelastic test cases. To illustrate the steady-state performance, all of the current test cases used 100 explicit time steps to start the calculation, followed by no more than 100 implicit time steps at a CFL number of 50 to drive the residual down at least six orders of magnitude. The unsteady solver is similarly considered efficient in the sense that the time step was chosen for time-accuracy considerations only, resulting in around 70 time steps per cycle of response for the Goland wing.

First, the cost of the direct method for the AGARD wing using an approximate Jacobian matrix was 1.87 times the steady-state cost. In the current work, using the exact Jacobian, this cost has gone up to 4.16. The reason for this is the cost of the preconditioning, with two levels of fill-in required to solve the linear systems effectively. Hence, although quadratic convergence is obtained, reducing the number of Newton steps, the overall cost has increased. To offset this disadvantage, the inverse power method is now available and performs very well, with the cost again dominated by the preconditioning. However, the complex variable form of the preconditioner is much more compact and requires less fill-in (and hence cost).

Secondly, the cost of computing the LCOs of the Goland wing by the full-order system is very significant. The full-system time marching can take many hundreds of cycles to reach the limit cycle, especially close to the bifurcation point. The computation using the reduced model has several stages for which the cost is summarized in Table 2. First, the inverse power method is used to map out the behavior of the eigenvalues. This requires multiple applications of the inverse power method with different shifts; for each of the four structural modes, six dynamic pressures were computed, giving a cost of 130 steady-state calculations. It was then quick to compute the bifurcation point using the direct method and to generate the two-degree-of-freedom model. Overall, the cost of generating the reduced model is less than 170 steady-state calculations. If the critical frequency is known in advance, then the inverse power part of the calculation can be skipped, substantially reducing the computational cost. Once the model is computed, it is parametrized, and so can be used to replace multiple unsteady full-system calculations. The reduction in computational cost, even when the inverse power

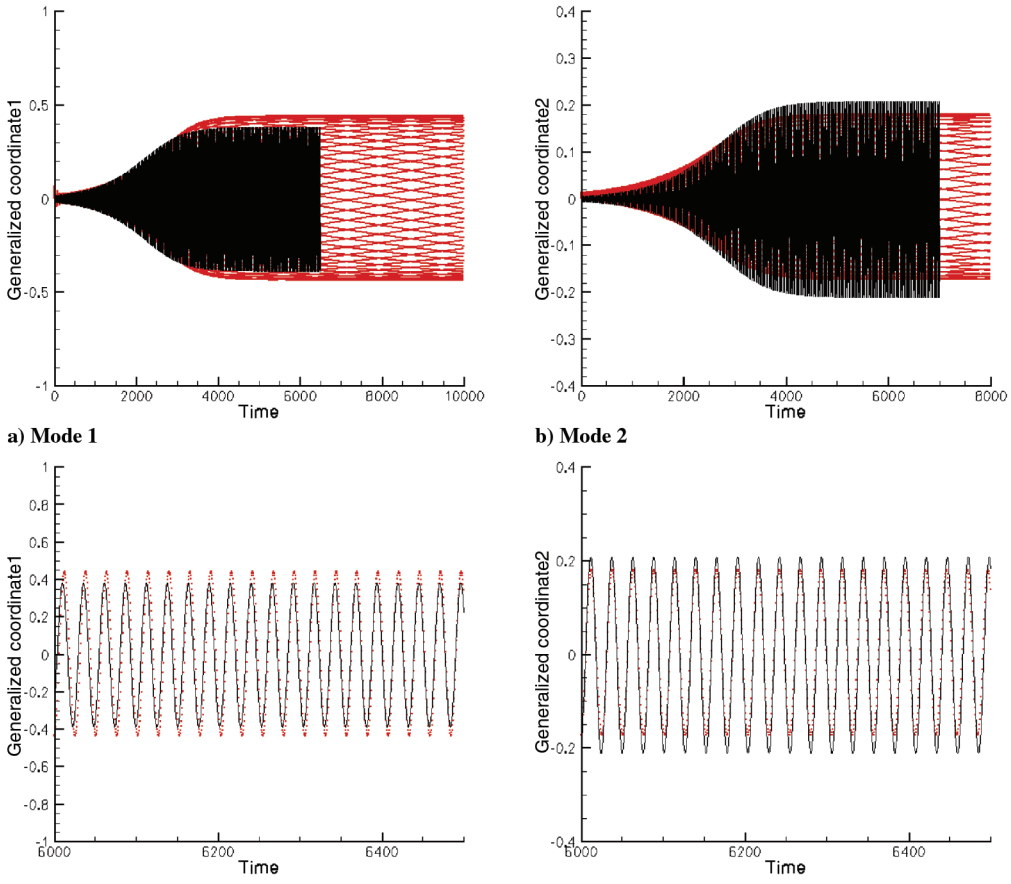

a) Mode 1 b) Mode 2

c) Mode 1, LCO region d) Mode 2, LCO region

Fig. 9 Comparison between the full and reduced predictions of LCO at 125% of the critical dynamic pressure for the Goland wing at Mach 0.92; symbols are from the simulation of the full system and lines are from the reduced model.

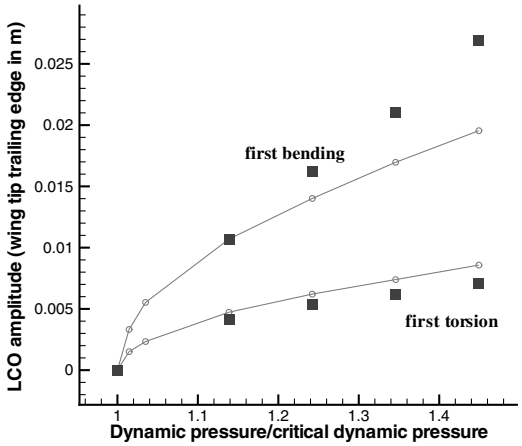

Fig. 10 Growth of the LCO amplitude in the first and second modes at Mach 0.92 for the Goland wing; filled squares are from the simulation of the full system and the line is from the reduced model.

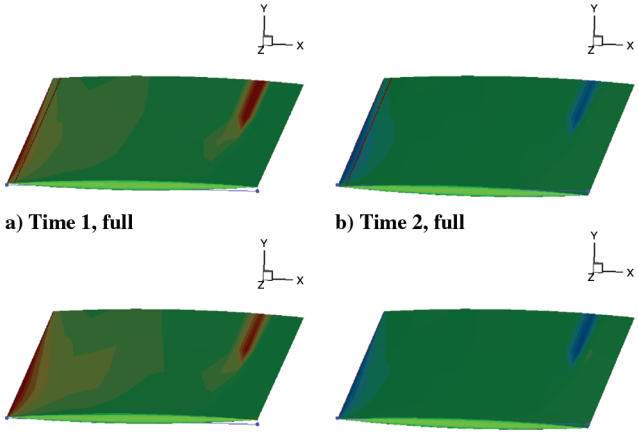

a) Time 1, full **b) Time 2, full**

c) Time 1, ROM **d) Time 2, ROM**

Fig. 11 Response at extremes of the wing at 1.35 times the critical value of dynamic pressure using the reduced and full models. The undeflected tip position of the wing is indicated by the blue line joining two dots at the wing tip, and the surface contours shown are for change of pressure from the equilibrium value. These results are for the Goland wing at Mach 0.92.

calculation is required, is by two orders of magnitude when several LCO calculations are required.

Conclusions

This paper has provided a formulation of three methods to allow aeroelastic analysis based on CFD-generated aerodynamics. The inverse power method and the direct method allow the investigation of stability of the system without resorting to time-domain analysis. If little is known about the instability onset, then the inverse power method can be used to map out the behavior of the eigenvalues in the regions likely to be of interest. This information can then be used to set up a direct calculation of the flutter point, along with other information such as the critical eigenvector and the frequency of the instability. In turn, this information can then be used to compute a two-degree-of-freedom model for the system dynamics around the bifurcation point, including limit-cycle responses.

The key numerical techniques that facilitate these methods were described. First, the ability to generate analytical first Jacobians of the second-order spatial CFD discretization is crucial and was described. This advance on previous work opens up the possibility of applying the inverse power method to compute the eigensystem behavior. Secondly, the model reduction requires the formation of matrix-vector products against the second and third Jacobians of the system. This is achieved through the use of matrix-free products using extended-order arithmetic. Finally, a Krylov-type method is used to solve the sparse linear systems that are featured in all three methods.

The methods were tested on three wing cases. The AGARD wing provided continuity with previous work. The MDO wing exercised the inverse power method and included the effect of a static deflection, and the Goland wing case featured the computation of a limit-cycle oscillation. All three cases were computed on relatively coarse grids, but it was argued that in all three cases, the behavior is representative for the test cases and provides a test for the methods.

Future work now includes the application of the methods to full aircraft test cases on fine grids. A Jacobian matrix for a grid with 17 million grid points was successfully formed on a 48-processor cluster with a memory of 48 Gb. The major challenge of forming an effective preconditioner for the parallel solution of linear systems is ongoing.

Table 2 Summary of the costs expressed in multiples of the steady-state solution

Case	Steady	IPM	Root locus	Direct	Unsteady
AGARD	1	1.1	100	4.2	45
MDO	1	3.2	154	24.7	200
Goland	1	5.4	130	9.2	1000

Acknowledgements

This work was supported by BAE Systems, the Engineering and Physical Sciences Research Council, the Department of Trade and Industry, and the Ministry of Defence and is part of the work program of the Partnership for Unsteady Methods in Aerodynamics (PUMA) Defence and Aerospace Research Partnership (DARP).

References

[1] Denegri, C. M., Dubben, J. A., and Maxwell, D. L., "In-Flight Wing Deformation Characteristics During Limit Cycle Oscillations," *Journal of Aircraft*, Vol. 42, No. 2, 2005, pp. 500–508.

[2] Thomas, J. P., Dowell, E. H., Hall, K. C., and Denegri, C. M., "An Investigation of the Sensitivity of F-16 Fighter Flutter Onset and Limit Cycle Oscillations to Uncertainties," 47th AIAA/ASME/ASCE/AHS/ASC Structures. Structural Dynamics and Materials Conference, Newport, RI, AIAA Paper 2006-1847, May 2006, pp. 511–522.

[3] Dreim, D. R., Jacobsen, S. B., and Britt, R. T., "Simulation of Non-Linear Transonic Aeroelastic Behavior on the B2," *CEAS/AIAA/ICASE/NASA Langley International Forum on Aeroelasticity and Structural Dynamics*, CP-1999-209136, NASA Langley Research Center, Hampton, VA, 1999.

[4] Farhat, C., Geuzaine, P., and Brown, G., "Application of a Three-Field Nonlinear Fluid-Structure Formulation to the Prediction of the Aeroelastic Parameters of an F-16 Fighter," *Computers and Fluids*, Vol. 32, No. 3, 2002, pp. 3–29.

[5] Melville, R., "Nonlinear Simulation of F-16 Aeroelastic Instability," 39th AIAA Aerospace Sciences Meeting, Reno, NV, AIAA Paper 2001-0570, 2001.

[6] Pranata, B. B., Kok, J. C., Spekreijse, S. P., Hounjet, M. H. L. and Meijer, J. J., "Simulation of Limit Cycle Oscillation of Fighter Aircraft at Moderate Angle of Attack," *Proceedings of the International Forum on Aeroelasticity and Structural Dynamics* [CD-ROM], Nederlandse Verening voor Luchtvaarttechniek, Amsterdam, Oct. 2003.

[7] Lucia, D. J., Beran, P. S., and Silva, W. A., "Reduced-Order Modeling: New Approaches for Computational Physics," *Progress in Aerospace Sciences*, Vol. 40, Nos. 1–2, 2004, pp. 51–117.

[8] Thomas, J. P., Dowell, E. H., and Hall, K. C., "Three-Dimensional Transonic Aeroelasticity Using Proper Orthogonal Decomposition-Based Reduced-Order Models," *Journal of Aircraft*, Vol. 40, No. 3, 2003, pp. 544–551.

[9] Lucia, D., Beran, P. S., and Silva, W., "Aeroelastic System Development Using Proper Orthogonal Decomposition and Volterra Theory,"AIAA Paper 2003-1922, 2003.

[10] Morton, S. A., and Beran, P. S., "Hopf-Bifurcation Analysis of Airfoil Flutter at Transonic Speeds," *Journal of Aircraft*, Vol. 36, 1999, pp. 421–429.

[11] Badcock, K. J., Woodgate, M. A., and Richards, B. E., "The

Application of Sparse Matrix Techniques for the CFD Based Aeroelastic Burcation Analysis of a Symmetric Aerofoil," *AIAA Journal*, Vol. 42, No. 5, May 2004, pp. 883–892.

[12] Badcock, K. J., Woodgate, M. A., and Richards, B. E., "Direct Aeroelastic Bifurcation Analysis of a Symmetric Wing Based on the Euler Equations," *Journal of Aircraft*, Vol. 42, No. 3, 2005, pp. 731–737.

[13] Woodgate, M. A., and Badcock, K. J., "A Reduced Order Model for Damping Derived from CFD Based Aeroelastic Simulations," 47th AIAA/ASME/ASCE/AHS/ASC Structures. Structural Dynamics and Materials Conference, Newport, RI, AIAA Paper 2006-2021, May 2006.

[14] Woodgate, M. A., Badcock, K. J., Rampurawala, A. M., Richards, B. E., Nardini, D., and Henshaw, M. J., "Aeroelastic Calculations for the Hawk Aircraft Using the Euler Equations," *Journal of Aircraft*, Vol. 40, No. 4, 2005, pp. 1005–1012.

[15] Rampurawala, A. M., and Badcock, K. J., "Treatment of Complex Configurations for Flutter Calculations," 47th AIAA/ASME/ASCE/AHS/ASC Structures. Structural Dynamics and Materials Conference, Newport, RI, AIAA Paper 2006-2077, May 2006.

[16] Badcock, K. J., Richards, B. E., and Woodgate, M. A., "Elements of Computational Fluid Dynamics on Block Structured Grids Using Implicit Solvers," *Progress in Aerospace Sciences*, Vol. 36, Nos. 5–6, Aug. 2000, pp. 351–392.

[17] Osher, S., and Chakravarthy, S., "Upwind Schemes and Boundary Conditions with Applications to Euler Equations in General Geometries," *Journal of Computational Physics*, Vol. 50, No. 3, June 1983, pp. 447–481.

[18] Van Leer, B., "Towards the Ultimate Conservative Conservative Difference Scheme 2: Monotonicity and Conservation Combined in a Second Order Scheme," *Journal of Computational Physics*, Vol. 14, No. 4, Mar. 1974, pp. 361–374.

[19] Jameson, A., "Time Dependent Calculations Using Multigrid, with Applications to Unsteady Flows Past Airfoils and Wings," AIAA Paper 91-1596, 1991

[20] Goura, G. S. L., "Time Marching Analysis Of Flutter Using Computational Fluid Dynamics," Ph.D. Thesis, Univ. of Glasgow, Glasgow, Scotland, U.K., Nov. 2001.

[21] Goura, G. S. L., Badcock, K. J., Woodgate, M. A., and Richards, B. E., "Extrapolation Effects on Coupled CFD-CSD Simulations," *AIAA Journal*, Vol. 41, No. 2, 2003, pp. 312–314.

[22] Tsai, H. M., Wong, A. S. F., Cai. J., Zhu, Y., and Liu, F., "Unsteady Flow Calculations with a Parallel Multiblock Moving Mesh Algorithm," *AIAA Journal*, Vol. 39, No. 6, 2001, pp. 1021–1029.

[23] Gaitonde, A. L., and Fiddes, S. P., "A Three-Dimensional Moving Mesh Method for the Calculation of Unsteady Transonic Flows," *The Aeronautical Journal*, Vol. 99, No. 984, 1995, pp. 150–160.

[24] Seydel, R., "Practical Bifurcation Analysis and Stability Analysis," 2nd ed., Springer-Verlag, New York, 1994.

[25] Golub, G. H., and Van Loan, C. F., *Matrix Computations*, John Hopkins Univ. Press, Baltimore, MD, 1996.

[26] Eisenstat, S. C., Elman, H. C., and Schultz, M. H., "Variational Iterative Methods for Nonsymmetric Systems of Linear Equations," *SIAM Journal on Numerical Analysis*, Vol. 20, No. 2, 1983, pp. 345–357.

[27] Girodroux-Lavigne, P., Grisval, J. P., Guillemot, S., Henshaw, M., Karlsson, A., Selmin, V., Smith, J., Teupootahiti, E., and Winzell, B., "Comparison of Static and Dynamic Fluid-Structure Interaction Solutions in the Case of a Highly Flexible Modern Transport Aircraft Wing," *Aerospace Science and Technology*, Vol. 7, No. 2, Mar. 2003, 121–133.

[28] Allen, C. B., Jones, D., Taylor, N. V., Badcock, K. J., Woodgate, M. A., Rampurawala, A. M., Cooper, J. E., and Vio, G. A., "A Comparison of Linear and Nonlinear Flutter Prediction Methods: A Summary of PUMA DARP Aeroelastic Results," *The Aeronautical Journal*, Vol. 110, No. 1107, May 2006, pp. 333–343.

[29] Beran, P. S., Knot, N. S., Eastep, F. E., Synder, R. D., and Zweber, J. V., "Numerical Analysis of Store-Induced Limit Cycle Oscillation," *Journal of Aircraft*, Vol. 41, No. 6, 2004, pp. 1315–1326.

[30] Synder, R. D., Scott, J. N., Knot, N. S., Beran, P. S., and Zweber, J. V., "Predictions of Store-Induced Limit Cycle Oscillations Using Euler and Navier-Stokes Fluid Dynamics," AIAA Paper 2003-1727, Apr. 2003.

[31] Knot, N. S., Beran, P. S., Zweber, J. V., and Eatsep, F. E., "Influence of Tip Store Mass Location on Wing Limit-Cycle Oscillation," AIAA Paper 2003-1731, 2003.

[32] Parker, G. H., Maple, R. C., and Berans, P. S., "Analysis of Store Effects on Limit Cycle Oscillation," AIAA Paper 2006-1846, 2006.

E. Livne
Associate Editor